UCLA
UCLA Electronic Theses and Dissertations

Title

Non-periodic Metasurfaces for Blazing and Metasurface Assisted Leaky Waveguide

Permalink

Author

Tao, Cheng

Publication Date

2017

UNITVERSITY OF CALIFORNIA

Los Angeles

Non-periodic Metasurfaces for Blazing and Metasurface Assisted

Leaky Waveguide

A thesis submitted in partial satisfaction

of the requirements for the degree Master of Science

in Electrical Engineering

by

Cheng Tao

2017

ABSTRACT OF THE THESIS

Non-periodic Metasurfaces for Blazing and Metasurface Assisted Leaky

Waveguide

by

Cheng Tao

Master of Science in Electrical Engineering Department

University of California, Los Angeles, 2017

Professor Tatsuo Itoh, Chair

In the first part of this thesis, non-periodic metasurfaces are explored to realize blazing effects

under oblique plane-wave illumination. Genetic Algorithm is used to optimize the surface's

local reflection phase over the entire finite aperture, for a particular scattering response (e.g.

blazing). Such non-periodic and random surfaces can open doors for the design of blazing

surfaces beyond typical periodic gratings and their limitations, e.g. reducing and flattening of

side-lobe levels, as well as other scattered beam characteristics such as beam-splitting. The

theoretical method is verified by full-wave electromagnetic simulations at X-band, and

measurements.

In the second part, a novel leaky waveguide is proposed which is assisted by

metasurfaces. This waveguide can support a half TE_{10} mode using a perfect magnetic

conductor for one wall, and therefore is more compact in size. The principle of operation and the dispersion diagram are then presented. The structure has the advantage of being simple, low cost, easy to fabricate, and requiring no vias, pins, or dielectric blocks. The guided wave shows leakage (radiative loss) along propagation by spilling energy to the orthogonal polarization (parallel plate mode) and radiating into free space from the sides. Based on this, one potential leaky wave antenna application is proposed.

The thesis of Cheng Tao is approved.

Benjamin S. Williams

Yuanxun Wang

Tatsuo Itoh, Committee Chair

University of California, Los Angeles

2017

To my beloved families.

TABLE OF CONTENTS

TABLE OF FIGURES

ACKNOWLEDGEMENT

First and foremost, I wish to express my deep gratitude to my Master's supervisor, Professor Tatsuo Itoh. It has been my great honor to be his student. I appreciate his guidance and supervision over the year to make my master experience productive.

I would also like to thank Doctor Mohammad Memarian. His hands-on guidance helped me through numerous problems in my projects and gave me good insights into how to do research.

I want to thank my colleagues at Microwave Electronics Lab, Kirti, Xiaoqiang, Yasuo and Haozhan. They helped me a lot during my master study and research. It was great pleasure to work with them.

Last but not least, I would like to thank my parents. Without their love and support, none of this would ever have happened to me.

Chapter 1

Non-periodic Metasurfaces for Blazing and Beam Splitting

1.1 Introduction

1.1.1 Metasurfaces

Metamaterials are generally referred to materials engineered to have properties not found in nature. As one important type of metamaterials, metasurface is typically a composite material layer engineered by an array of small scatterers or apertures designed to control the behaviors of physical fields in radio, microwave, terahertz, optical and other regimes of the electromagnetic spectrum [1-3]. The properties of metasurfaces are usually not unattainable in nature materials, such as negative refractive index type behavior, and generalized Snell's law of refraction [4, 5]. The layer thickness is negligible compared to the wavelength. The elements to form the building blocks of metasurfaces are typically resonant elements with dimension of subwavelength scale. By specifically modifying the subwavelength element, the metasurfaces can be made to control the propagation or scattering properties of surface or planar wave.

Compared to conventional metamaterials, which are usually 3D structures, metasurfaces have the advantages of being compact, easy to fabricate, and can be potentially engineered as less-lossy structures. The applications of metasurfaces also cover a wide range of electromagnetic applications from microwave to optics, including electromagnetic absorbers [6], novel waveguide structures [1], blazing metamaterials and metasurfaces [7-9], to name a few.

1.1.2 Blazing

Blazing or retro-reflection of a wave obliquely incident on a surface has classically been realized with periodic gratings. Fig. 1 shows some classical periodic blazed gratings on finite size apertures, such as right-angle sawtooth [10] (a.k.a echelette) in Fig. 1 (a), and other 3D structures (e.g. groove gratings [11, 12]). These structures have been widely used in microwaves and optics for different applications. Recently with the advent of metasurfaces [5], metasurface based blazed gratings, such as the ones shown in Fig. 1 (b) and (c), have also been experimentally demonstrated [7, 13, 14]. In metasurface gratings, with the combination of grating effect and metasurface concepts, the design of the unit-cell is done in a planar fashion using either phase-modulating elements in the cell [7, 13] or planar resonant cells [14]. In practice, gratings are placed on the finite aperture, whose size may be in the order of tens, hundreds to millions of periods long, depending on the application and frequency. The smaller the grating aperture is, the more the backscattered wave appears as a broadened lobe in the pattern corresponding to the aperture size and beam width trade-off.

In this chapter, we depart from this classic thinking of using periodic gratings to produce blazing effects from a finite aperture, as shown in Fig 1 (d). Instead, a non-periodic method is used to attain the same blazing objective. The perspective is to treat the entire finite scattering aperture as a whole, and design it to perform the particular scattered beam behavior. The total scattering aperture therefore does not necessarily need to be periodic. It also does not necessarily use the m=-1 mode of a periodic structure and the so-called Bragg condition [2] to achieve back reflection of the oblique incident beam. The entire aperture is tailored to achieve the desired scattering behavior (say blazing, or power splitting, etc.), without being

restricted to the grating equation and operation. Consequently, one may outperform the

characteristics of finite size periodic 3D [10, 11] and metasurface [7, 13, 14, 15] based

gratings or attain scattering behavior that is not achievable with such periodic structures.
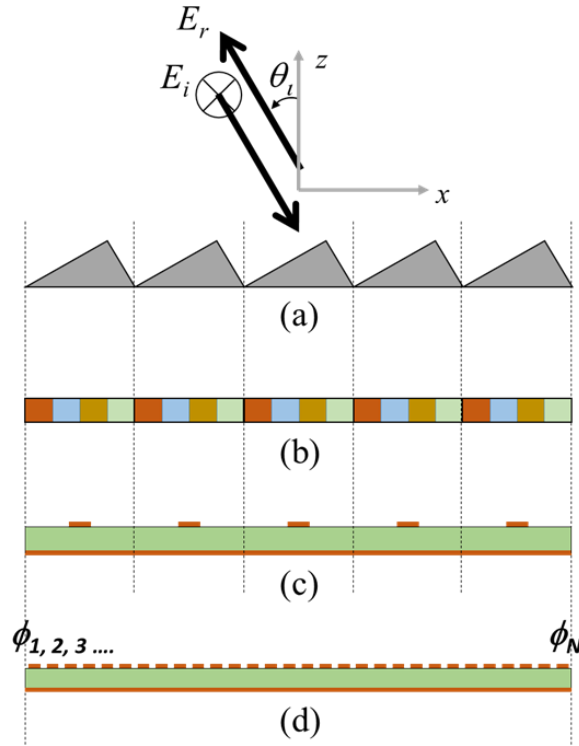
Figure 1   A finite scattering aperture realized with periodic blazed gratings (a) classic sawtooth [10] (b)

planar metasurface [7, 13]. (c) planar resonant metasurface [14] periodic gratings. (d) A non-periodic

metasurface of same aperture size.

The non-periodic metasurface phase response for each element is designed using

optimization techniques. The optimization is performed on an antenna array model of the

scattering scenario that takes place. Genetic Algorithm (GA) is used to perform optimization

on phase of the discrete elements of the aperture, in order to attain a desired scattered pattern.

3

GA has been used in the past for tailoring of radiation patterns of phased antenna arrays and sparse arrays [15]. Two cases, a blazing retroreflective beam (similar to a periodic grating), as well as a beam splitter are demonstrated in this chapter.

1.2 Theory and Methodology

1.2.1 Periodic Blazed Gratings

As a result of the Floquet theory, the governing equation of operation of a one dimensional grating for propagating waves in vacuum with period (d), diffracted order (m), operating wavelength (λ_0), incidence angle (θ_i), and diffracted order angle (θ_m) should satisfy

$$\sin\theta_i + \sin\theta_m = \frac{m\lambda_0}{d} \qquad (1.1)$$

For retro-reflection of the wave (a.k.a Littrow condition or auto-collimation), the periodicity of the grating must be chosen to force the higher order mode (typically the m = -1) to be in the direction of incidence, thus satisfying

$$kd\sin\theta_i = \pi \qquad (1.2)$$

This is also known as the Bragg condition [11], causing the m=-1 beam to be directed back in the path of incidence. Thus, the period of all such blazed gratings (either planar or non-planar) is large, and in the order of one free-space wavelength (e.g. for θ_i=30°, d=λ_0). The design of periodic blazed gratings (be it the classical 3D or the planar metasurface cases) then boils down to design of the grating unit-cell. This determines what portion of the incident power scatters into the m=-1 mode, and how much scatters into the specular m=0 mode, as the specular mode is always a valid solution in (1.1).

The existence of specular reflection is normally a challenge with periodic blazed gratings, which has led to a great body of literature on grating efficiency […]. In addition, when a finite size blazed grating is used to retro-reflect a beam, the resulting backscattered beam is broadened, with side lobes, some of which are potentially very significant and close to the main beam. This is especially the case at microwaves, where the finite aperture is in the order of tens or hundreds of periods. At optics, blazed gratings are much higher multiples of the period.

1.2.2 Non-periodic Blazed Metasurface

We model the scattering due to a reflective surface under oblique illumination, by discretizing the surface into sub-wavelength elements, and treating the re-radiation from this surface as array of radiating elements as shown in Fig 1 (d). Fig. 2 depicts the process of generating the theoretical response used by GA.
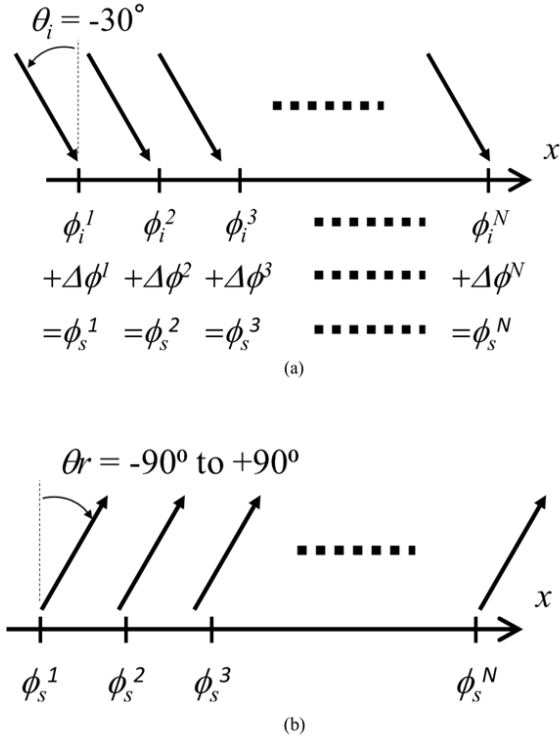
Figure 2   Modelling the scattering surface as the re-radiating scattering antenna array with plane wave

excitation.

At each location on the surface, the incidence angle of plane wave is known (e.g. angle

of incidence $\theta_i=30°$ in Fig. 2). This determines the excitation phase (excitation amplitude $= 1$

on the entire surface as plane-wave is used) of each element on the surface. The elements are

then required to provide a local phase-shift ($\Delta\phi_k$) at the k-th position, which is to be added to

the excitation phase. The local phase shift provided by each element can be characterized by

reactive impedance surface using transmission line model as shown in Fig. 3.
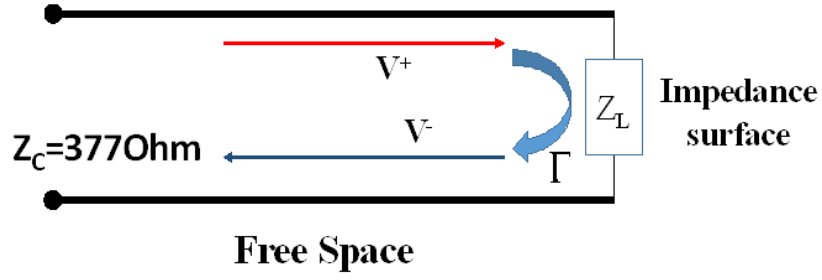
Figure 3   Transmission line model of reactive impedance surface

In this model, we assume that a normal incidence plane wave impinges on a metasurfaces. The reflection or scattering properties of the wave can be conveniently characterized with the transmission line model. The whole metasurface can then be regarded as a termination with impedance Z_L. The reflection coefficient Γ, which can be expressed by:

$$\Gamma = \frac{Z_L - Z_C}{Z_L + Z_C} \qquad (1.3)$$

Reflection wave can be expressed by:

$$V^- = \Gamma V^+ \qquad (1.4)$$

This reflection coefficient Γ is a complex number $\Gamma = Ae^{\phi}$ with amplitude A and phase response ϕ. Specifically, if $\phi = 180°$ and $A=1$, the reflection electric field is completely reversed in terms of incident field and thus this surface can be regarded as a perfect magnetic conductor (PMC) in this scenario. Generally, the phase shift of single element in a metasurface can be obtained by single cell simulation with periodic boundary conditions. This part will be discussed in detail in section 1.3.

If we consider the amplitude of the reflection coefficient for all elements as uniform or it is same for elements that construct the metasurface, only phase response of the element will

matter to the calculation of scattering field. The scattered far-field pattern can be obtained by superposition of the incidence phase and reflection coefficient phase for each local element. Considering the notation used for the incident plane wave phase and discretization step d_x ($d_x=\lambda_0/4$ chosen here), the far field radiation pattern is:

$$Pattern(\theta_r) = \sum_{k=1}^{N} e^{-jkd_x \sin(\theta_i)} e^{-j\Delta\phi^k} e^{-jkd_x \sin(\theta_r)} \qquad (1.5)$$

which is written as the radiation pattern of a linear antenna array. The GA is then set up to optimize k=1 to N element phase values (N=48 here). At each stage of the GA, the calculated total pattern is judged against a particular fit-function (cost function) for each generation in GA.

For retro-reflection, one carefully chosen fit function is:

$$F = \frac{\max\limits_{-90°\leq\theta_r\leq-37°,-25°\leq\theta_r\leq+90°} \{|Pattern(\theta_r)|^2\}}{\max\limits_{-36°\leq\theta_r\leq-24°} \{|Pattern(\theta_r)|^2\}} . \qquad (1.6)$$

The objective of the GA is to minimize this fit function F. Since -30° is the angle of incidence, -36° to -24° represent for the region for retro-reflection angle, by placing the pattern of this region to the numerator, blazing or retro-reflection beam can be elevated. On the other hand, unwanted reflection (including specular reflection) can be suppressed, as well as reduced first side lobe level (FSLL) can be achieve by placing corresponding pattern region to the numerator of fit function and then minimizing it. Compared to the methods of using periodic gratings to achieve blazing effect, this non-periodic metasurface method has more freedom to adjust the fit-function by elevating or suppressing the pattern for desired scattered angle region. Furthermore, one can even assign different weight in different regions

to achieve flexible goals.

The result of the GA output of this stage is shown in Fig. 4. The reduction of the FSLL

while maintaining the same back scatter characteristics compared to the grating, is achieved

in this example by paying a penalty of elevated SLL elsewhere in the pattern. The GA was

tailored to provide a uniform and minimized SLL anywhere outside the main beam, and thus

achieving the demonstrated pattern. The first SLL in a typical ideal grating for blazing at -30°

having the same finite aperture size (equivalent to 12λ_0) is also shown in the inset of Fig. 4.
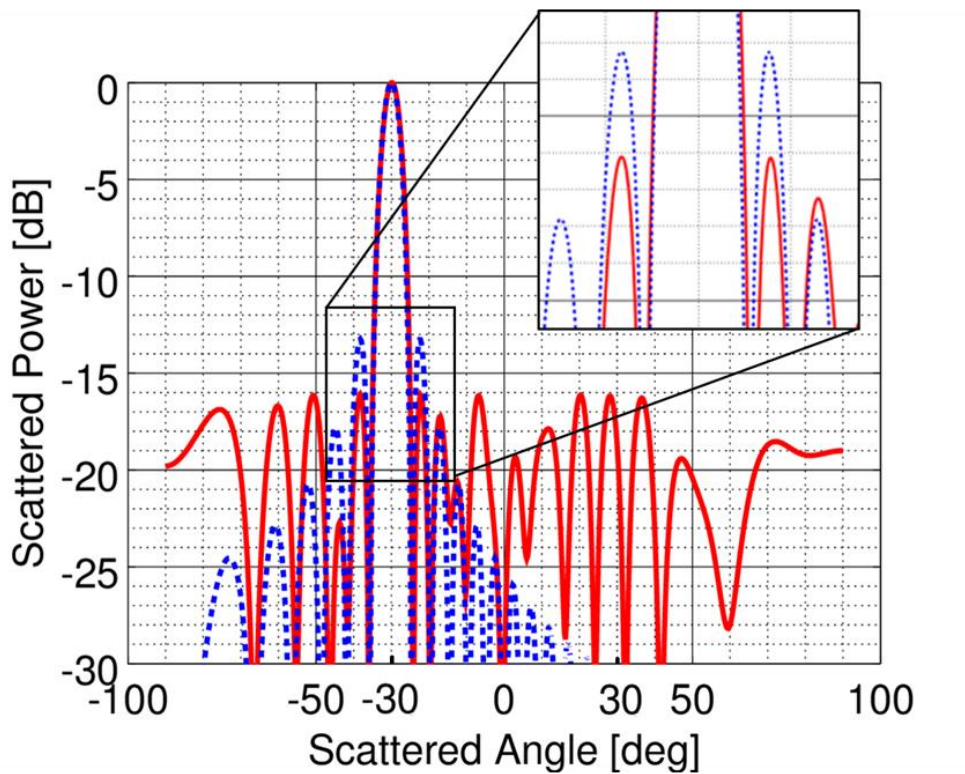

Figure 4   Theoretical response of blazed scattering from a periodic grating (dashed) and the

non-periodic surface optimized using GA (solid line).

The theoretical scattered array modelling approach taken here is particularly useful as one would otherwise need to optimize the entire elements of the overall surface (using GA or other methods) directly in the electromagnetic (EM) solver. The latter approach, can quickly become computationally unachievable using existing computing powers, especially as the number of elements is increased. An additional benefit is that practical phase limitations of the elements can be accounted for in the theory stage, to prescribe phase values that are suitable for the elements, as will be discussed in the design stage.

The main limitation of our theoretical modelling approach, however, is the accuracy of the model used for the scattering elements, which depends on how well the assumption of the radiation pattern for the single element holds in the actual structure with the existence of effect of mutual coupling between adjacent elements. Since the phase response is based on single cell simulation with periodic boundary condition, it can be regarded as the first order approximation of response of the single element. However, in the case of non-periodic metasurface, each element is more likely to have neighbor elements with different geometry or shape and the periodic boundary condition does not hold any more. The mutual coupling from two adjacent different elements can be regarded as second or higher order effects and is omitted in this method, which might cause some discrepancy in practice. Other higher order coupling effects are generally weak and have negligible influence on the far-field pattern.

One possible way to enhance the accuracy by adding this mutual coupling effect is to consider the electric current and magnetic current on the surface of single element [16, 17]. First, one can place any combination of three different elements in simulation and then

extract the surface current only from the middle element. Both single element response and coupling effect from the neighbors are embedded in the electric current and magnetic current. Vector potential would then be used to obtain the far field and the radiation pattern. However, the drawback is also obvious. It is significantly more time consuming since in each GA generation it is required to perform a Fourier transform to find the far field from the surface currents or near field. Moreover, to extract and sample the surface current, one needs to first simulate all the combinations of three elements, which would be complicated when the number N of available elements is large and the complexity is proportional to N^3. It might take large space to sampling current and take a large amount of time to optimize the fit function.

1.3 Design

Here we consider the design of a metasurface operating under the Transverse Electric (TE) polarization at 10 GHz. For the coordinates used in this thesis, the electric field is in the y-direction, and the plane of incidence is considered as the x-z plane, and the surface is oriented along x. The other polarization may also be designed using appropriate elements.

Consider the simple constituent element shown in Fig. 5 (a) for local phase modulation under TE polarization. These elements were previously used as subwavelength elements for constructing the unit cell of the blazed grating in [6]. A strip of width W is oriented along x on a Rogers RT 6010 substrate with relative dielectric constant 10.2 and loss tangent 0.002,

backed by a conductor. The thickness of the dielectric *h* is 1.9mm. The element is made to be periodic along *x* and *y* using periodic boundary conditions (PBC). This periodic subwavelength unit cell is simulated under oblique incidence from the top port, and the reflected wave is computed. The phase of the reflection coefficient de-embedded to the top metallization is used as a measure of the local scattered wave phase.
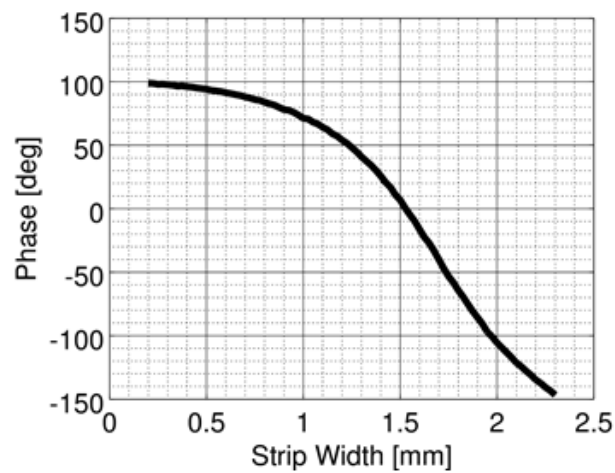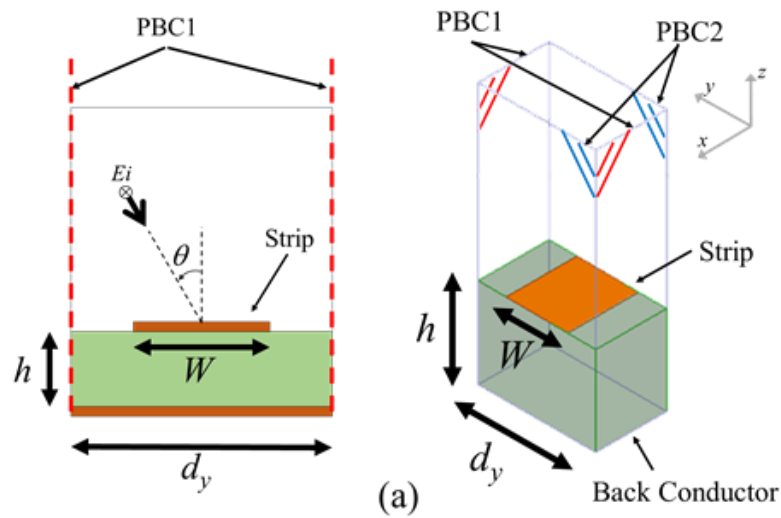
Figure 5 (a) unit-cell of the subwavelength scattering elements (b) phase of reflection coefficient at *z*=0 under

oblique incidence -30°, vs. strip width *W*.

Fig. 5 (b) shows the range of phase variation at 10 GHz as a function of strip width, for a transverse subwavelength period of $d_y = 2.5$ mm. The figure shows that elements can provide a reflection phase shift range between $-140°$ and $+100°$. The lower boundary phase $-140°$ is due to the minimum gap size (d_y-W) of 0.2mm based on typical limitations of fabrication attainable with etching, and the upper boundary phase $+100°$ corresponds to the case with the minimum strip size (W) (almost similar as no top metallization case), i.e. the reflection phase of a dielectric backed by the conductor.

As mentioned in previous section, these limitations of phase values can be considered in GA as boundaries for the N input variables. Thus, a new set of optimized elements are then calculated by GA with these phase constraints. Combined with the relation between phase and strip width depicted in Fig. 5(b), we can then translate these element phase data into strip widths for each element. The entire 48 elements metasurface is then constructed in the EM solver, and shined under an oblique -30° incident plane wave, and the scattered wave pattern is observed for -90° to +90°.

1.4 Simulation Results

1.4.1 Blazing / Retro-reflection Surface

Fig. 6 is one result for a non-periodic blazing metasurface at 10GHz resulting from our GA optimization design. The figure shows the top view of the metallization of the surface,

and its random nature along the *x*-direction and sub-wavelength periodic nature along the *y*-direction. EM simulation results of the designed non-periodic surface, with the design methodology described previously are also shown in Fig. 7. It can be seen that there exists a strong back-reflected beam directed towards the -30° direction. In addition, the first SLL of the beam is lower than -16dB.

In this design, elements 1 and 48 were forced to not contain any metallization to reduce strong edge scattering from the edges of the aperture, which can contribute to unwanted scattering artifacts.
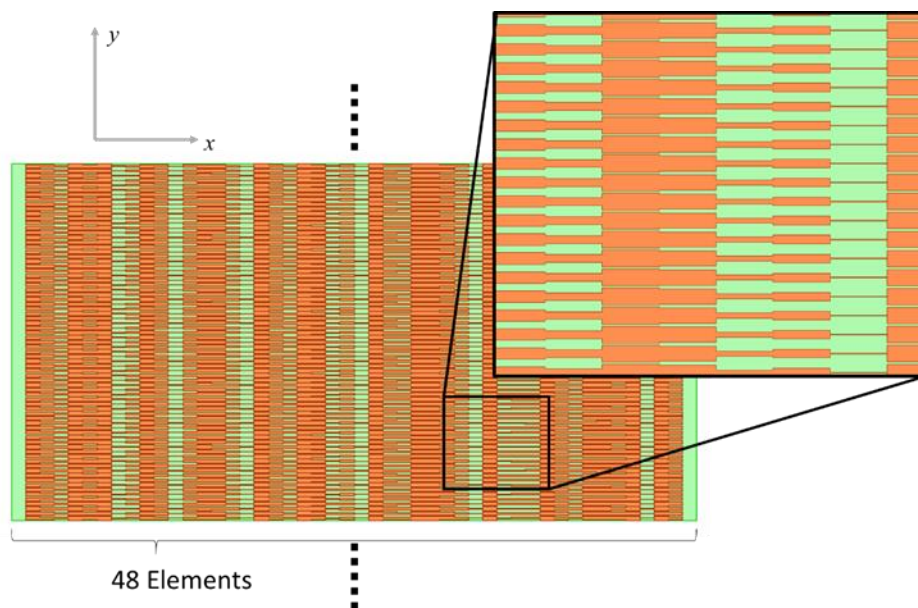
Figure 6   Top view of the simulated structure of the non-periodic metasurface being finite in *x*-direction and

infinitely periodic in *y*-direction

Figure 7　Scattered beam of the non-periodic blazing metasurface EM simulation result (solid line) and

theoretical GA output (dashed).

The main beam is optimized for -34° to -26°. We additionally observed that the actual

simulated structure always imposes a $\cos(\theta_r)$ like taper to the pattern, thus elevating radiation

in the broadside compared to end-fire directions. The reason for this is the limitations in the

simplified model used, which assumes an isotropic radiation pattern for each element. Thus,

we compensate for this inaccuracy of the theoretical model by further reducing SLL in the

theoretical response, which can be realized by assigning different weight factors at different

scattering angles in the fit function of GA. Therefore, we modified the GA fit function in

expression (4) with an additional constraint of having higher SLL reduction for angles -45° to

-35°, as well as -25° to +40° with a weighing factor of 5, compared to the regions -90° to -45°,

15

and +40° to +90°. As the model we assume only involves with local phase parameters, the optimization computation is quick which only takes several minutes. The EM simulation result seems to fairly match this theoretical result given by GA as shown in Fig. 7.Although we neglect the mutual coupling effect as mentioned in section 1.2, the main features of both radiation patterns including the beam width, FSLL as well as the locations of other side lobes are consistent in Fig. 7. This means our single element model is sufficiently reliable to predict and optimize the scattering behavior of the aperture.

1.4.2 Beam Splitting Surface

In the second example, we apply the GA to design a surface which scatters the same -30° incident wave into two beams. Again, one beam is aimed to have a similar blazing effect i.e. retro-reflect in the direction of incidence, while the second beam is directed towards broadside. The EM simulation results of the designed structure for 10GHz, based on phase values prescribed from GA outputs are depicted in Figure 8. From the figure, there are two beams centered at -30° and 0°, with effectively suppressed SLL for both theoretical GA result and EM simulation result. Such a surface can be applied to spatial power splitters.
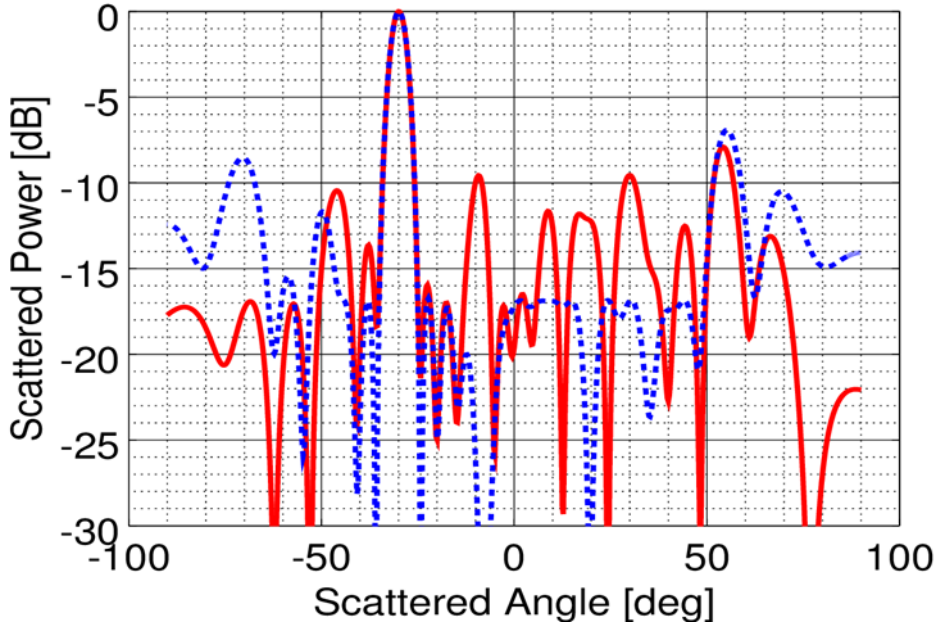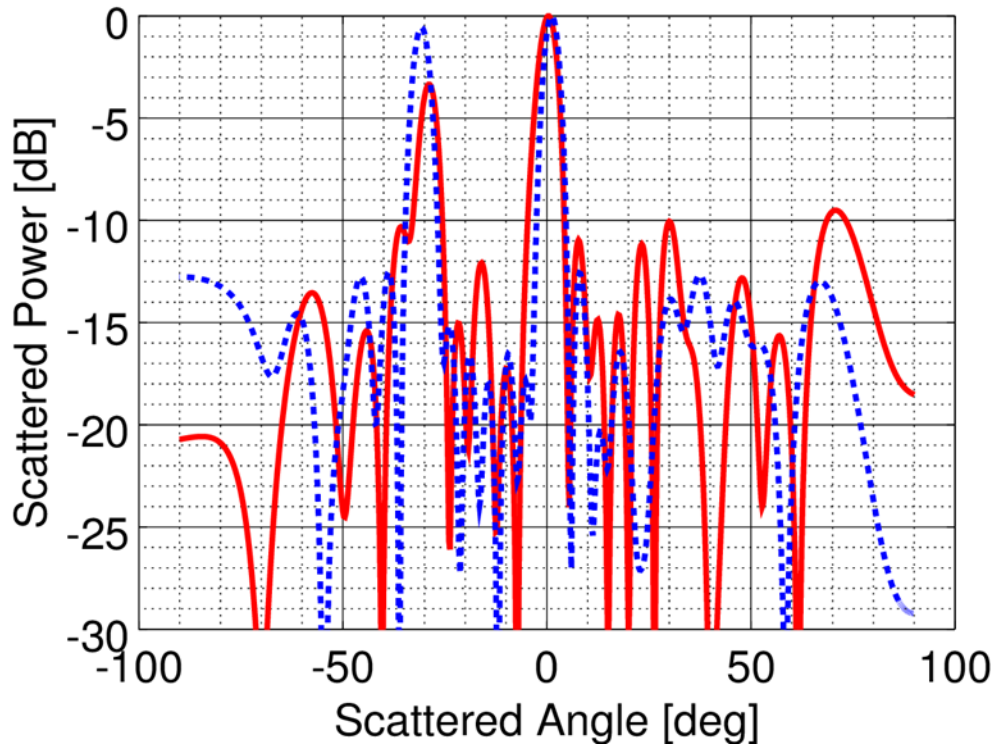
Figure 8　Scattered beam of the non-periodic beam splitting metasurface EM simulation result (solid

line) and theoretical GA output (dashed).

1.5 Fabrication Results

A sample of non-periodic metasurface for blazing was fabricated in UCLA Center for

High Frequency and Electronics (CHFE) through etching process with plotted mask. The

pattern of the mask same as shown in Fig. 6 is based on the optimized elements geometry

using genetic algorithm. A thin layer of photoresist was first applied on the Rogers RT 6010

board. This board was then exposed to UV light while covering with the mask. After

developing and baking, the board was put into etching solution (ferric chloride) to etch out the desired pattern for the non-periodic metasurface board. Fig. 9 is the fabricated board for non-periodic metasurface for blazing.
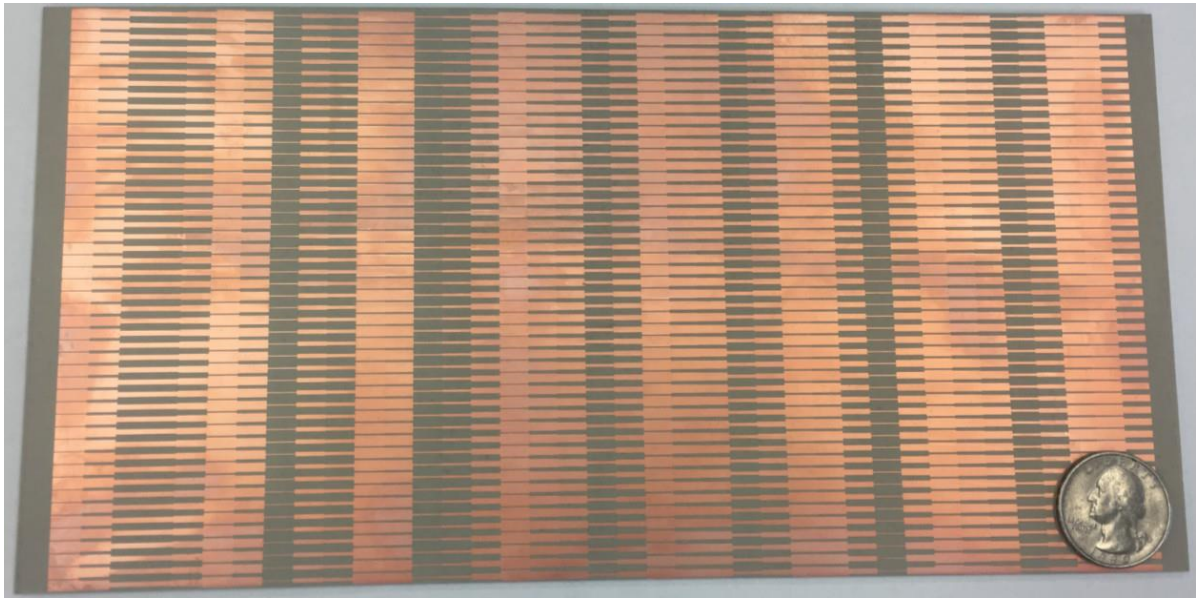
Figure 9   Non-periodic Metasurface for blazing

Before measuring the far-field pattern of this board, another simulation was carried out to sweep frequency from 9 GHz to 10 GHz to observe the far-field pattern for -30° incidence wave. Fig. 10 shows the patterns for frequency at 9 GHz, 9.3 GHz, 9.7 GHz and 10 GHz. Although we design this non-periodic metasurface at single frequency (10 GHz), the specular beams for this range of frequency are all suppressed under -10 dB. The main beam for 10 GHz locates at exact -30° retro-reflection angle, and as frequency decreasing to 9 GHz, the main beam gradually shifts towards endfire.
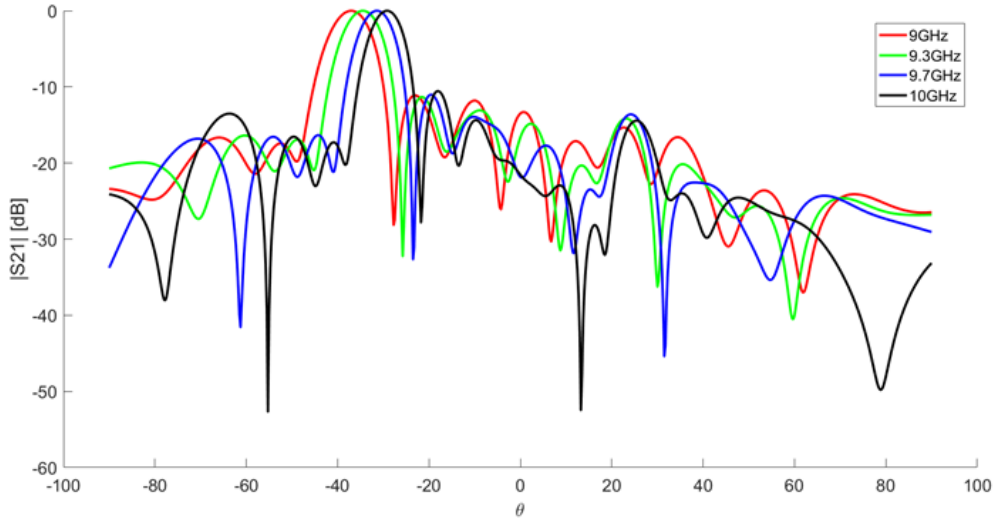
Figure 10   Far-field patterns for non-periodic metasurface at frequency 9GHz, 9.3GHz, 9.7GHz, and

10GHz

To compare with this simulation result, an experiment for measuring the far-field pattern of this fabricated board is set up as shown in Fig. 11. We use two horn antennas that are connected to port 1 and 2 of vector network analyzer (VNA) respectively as the transmitter and receiver for the measurement. As the incidence field is coupled into horn antenna as port 1 and radiate to far zone, the radiated field can be regarded as a TE polarized plane wave. This incidence wave is impinged onto the metasurface board which is also placed in the far field region. The scattering field re-radiated from the board is then received by the receiver. By rotating the receiver antenna, S_{21}, which is proportional to the scattering power received from different angles (ideally, θ_r ranging from -90° to 90°) can be measured. The

surroundings are covered with absorber for X-band to eliminate any scattering effects from

the environment.
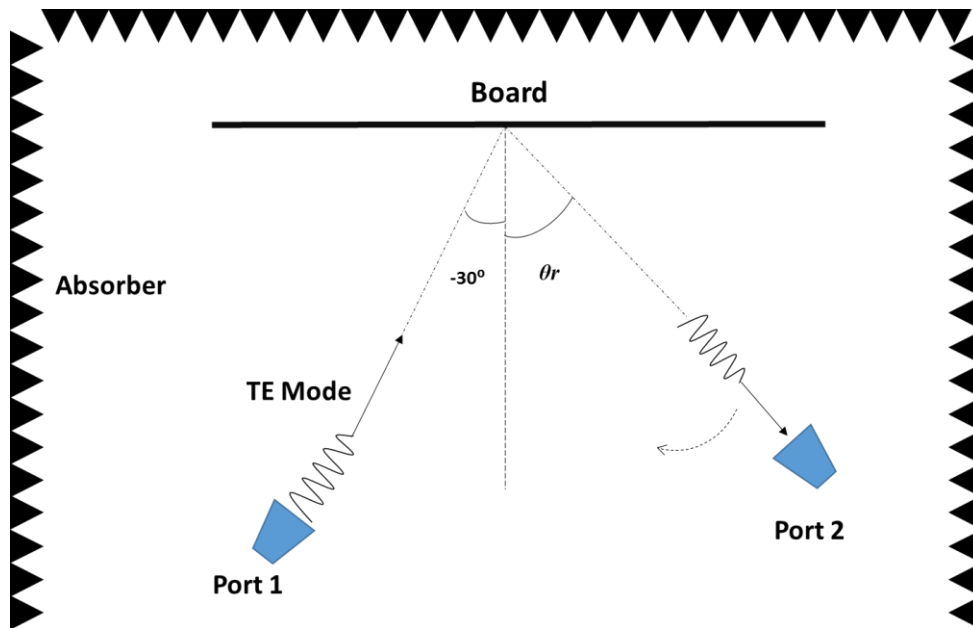
Figure 11   Experiment Set-up for far-field measurement of non-periodic metasurface

Fig. 12 shows the measured far-field patterns for non-periodic metasurface at 9 GHz, 9.3

GHz, 9.7 GHz, and 10 GHz, as well as a solid perfect electric conductor (PEC) board for

comparison. Fig. 13 is the pattern in polar coordinates. Metasurface patterns are marked as

solid curves and PEC pattern is marked as dash pink curve. As expected, the metasurface

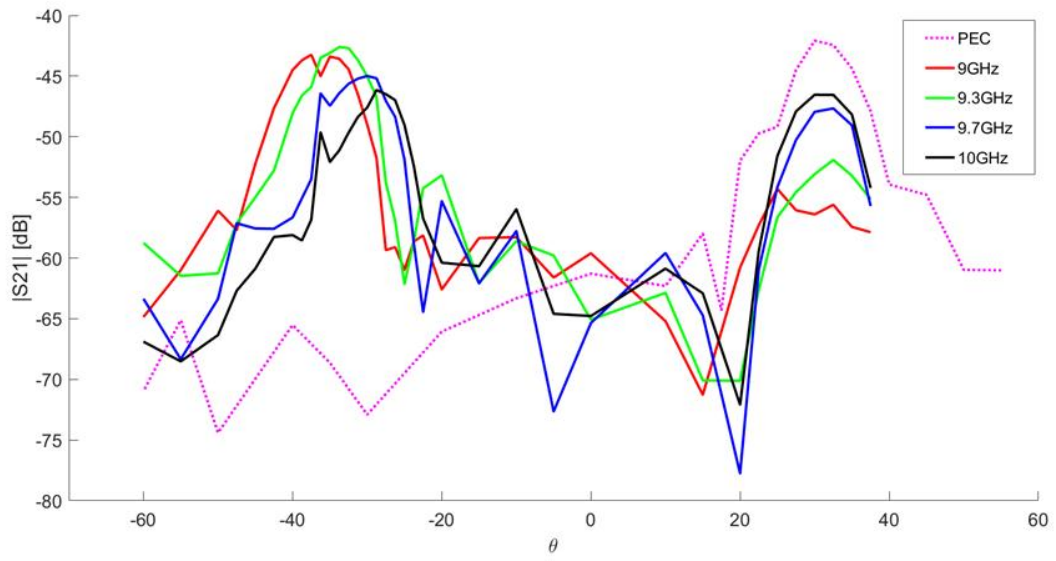provides blazing beam, while the solid PEC provides a specular beam only.

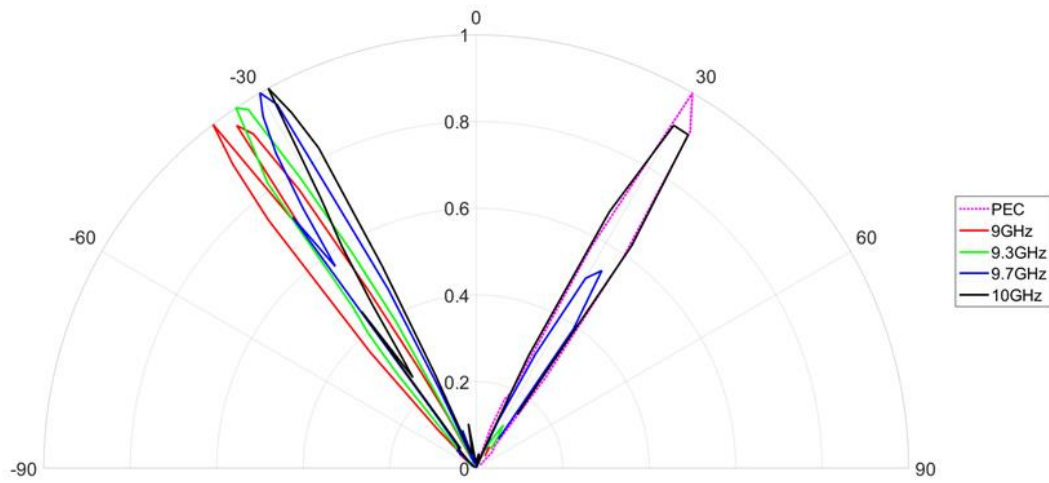Figure 12　Measured far-field pattern for non-periodic metasurface at different frequency

Figure 13　Measured far-field pattern for non-periodic metasurface at different frequency (polar plot)

From these two figures, the far-filed pattern of PEC (dash pink) shows only one beam which locates at specular angle. This satisfies reflection equation and the side lobes of this pattern is due to the finite aperture for PEC board. For the patterns of metasurface, the main beams all locate around -30°, which matches the simulation result in Fig. 10. As frequency shifts from 10 GHz to 9 GHz, the main beam shifts in the same trend as indicated in simulation. This means a large portion of electric field is scattered back to the incidence angle as blazing effect, which is not observed for PEC case. However, for metasurface pattern, especially at 10 GHz, there exists a large beam at around +30°, indicating part of the power is scattered in the specular direction. This specular beam is suppressed below -10 dB both in GA theoretical result and HFSS simulation, but in this measurement, it is in the comparable level with retro-reflection main beam. We attribute this discrepancy to the inaccuracy in the dielectric constant of fabrication board we use. Though the dielectric constant (dk) is labeled as 10.2 on the sample by the vendor, yet in practice 10.7 should be the correct value for designing according to the latest datasheet. We then apply all the design procedure from single cell simulation to full wave non-periodic board simulation with dk=10.7. The new single cell simulation is shown in Fig. 14.
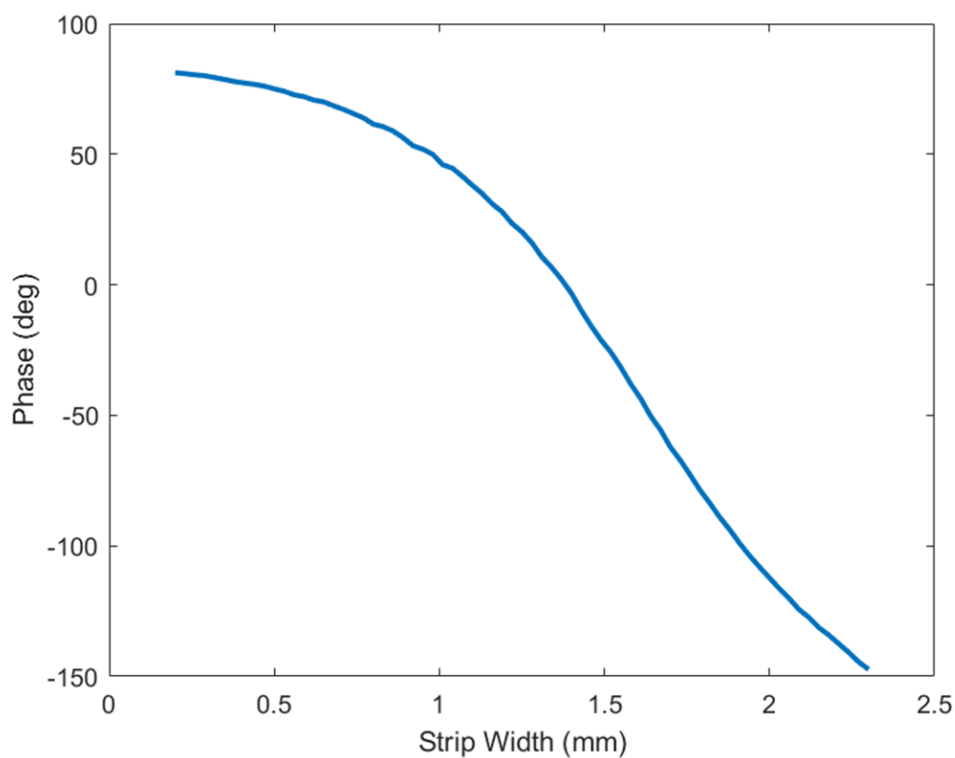
Figure 14   Single cell simulation for dielectric constant 10.7

The GA is again carried out to find the proper strip width for each element. The output results are then applied into HFSS simulation to generate far-field pattern for this non-periodic metasurface. Fig. 15 compares the pattern predicted by GA theoretical results and the pattern generated by HFSS simulation.
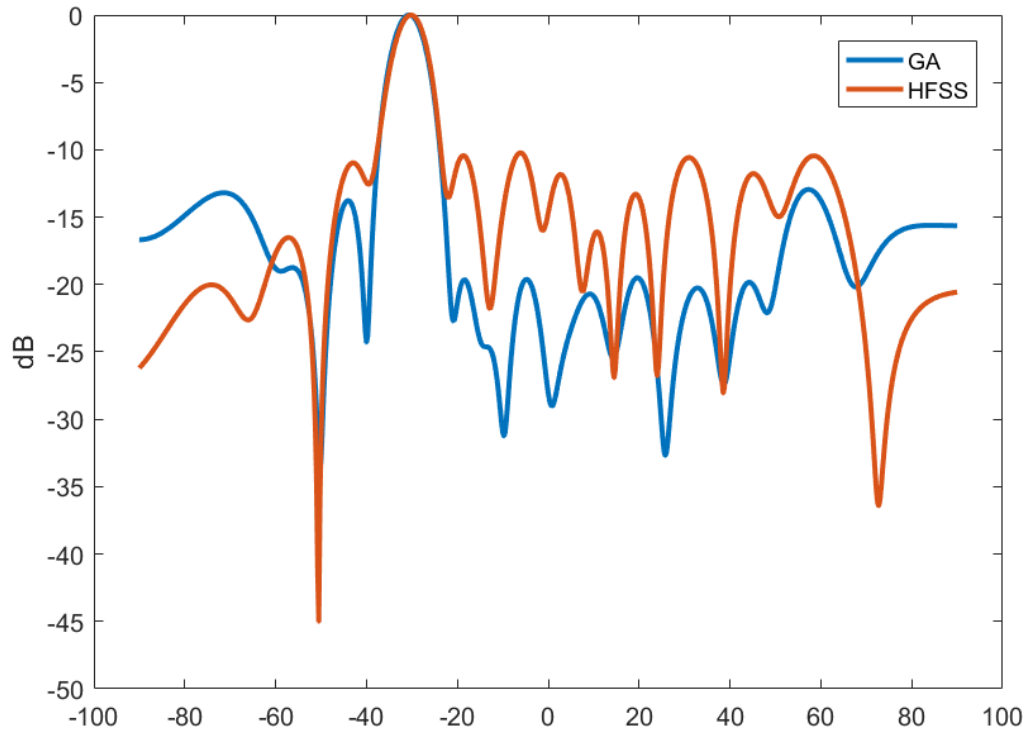
Figure 15   GA theoretical pattern vs HFSS simulation pattern for dielectric constant 10.7

From Fig. 15, the main features of two patterns still match very well, such as main beam locations and beamwidth. All side lobe levels are suppressed under -10 dB for both curves. The discrepancy of side lobe levels is because of the element phase model by neglecting mutual coupling effects as discussed in the previous section.

A new non-periodic metasurface board is then fabricated based on this simulation result. Fig. 16 shows the measured far-field pattern for 9-10 GHz with incidence wave at -30° angle.
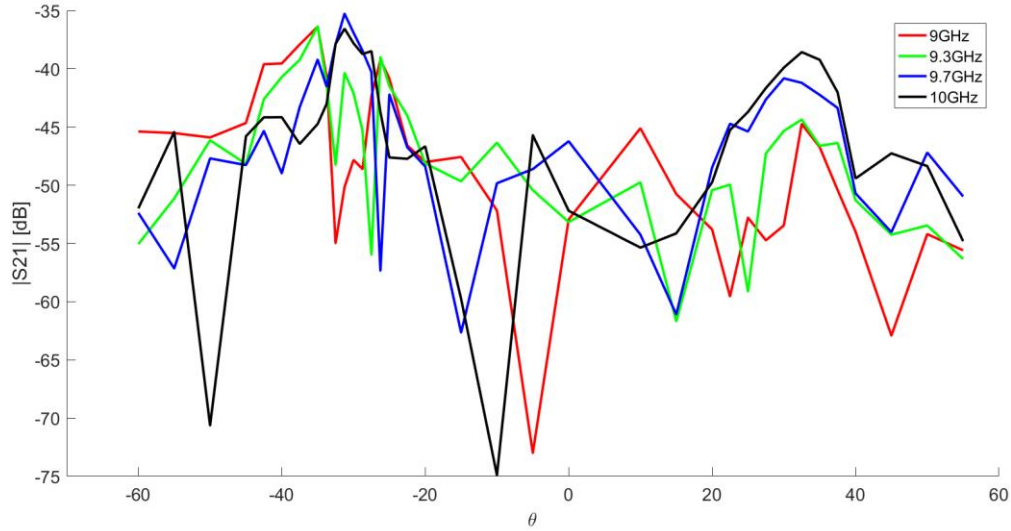
Figure 16　Measured far-field pattern for non-periodic metasurface with dielectric constant 10.7

From this figure, the main features of the patterns are similar to those in Fig. 12. For frequency at 10 GHz, the pattern still shows 2 main beams locating at blazing angle and specular angle respectively. In this case the specular beam is approximately 3 dB lower than the blazing beam, but for previous measurement shown in Fig. 12, two beams have the same level of amplitude. This improvement can be easily observed in the polar plot in Fig. 17.
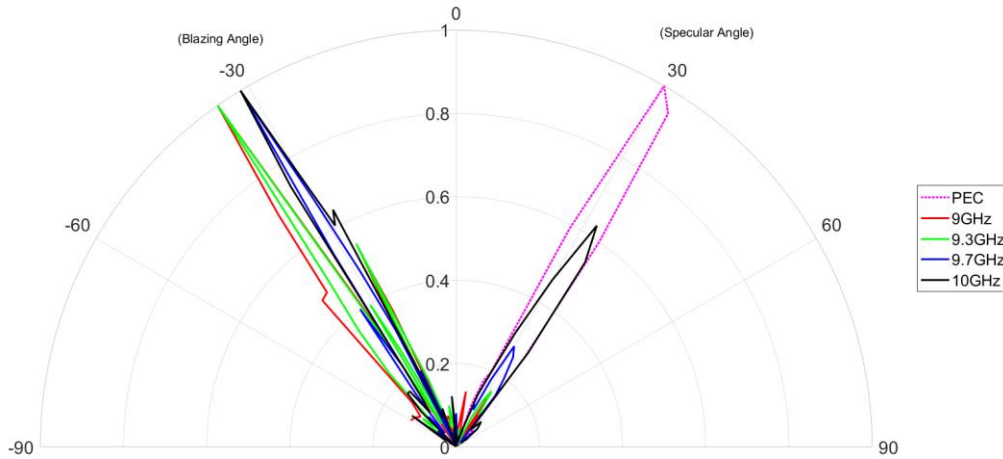
Figure 17　Measured far-field pattern for non-periodic metasurface with dielectric constant 10.7

Compared to Fig. 13, the specular beam of 10 GHz is suppressed, while the blazing beam still points towards -30° angle. Although discrepancy still exists between this measurement result and simulation result due to the factors such as finite size of fabricated board, fabrication error (over etching), the main properties of this non-periodic board is observed, i.e., scattering the main beam back to the incidence angle as well as suppressing the specular beam.

Chapter 2

Metasurface Assisted PMC-PEC Waveguide

2.1 Introduction

Since the advent of metamaterials, several metamaterial based waveguides, such as the gap waveguide, have been experimentally demonstrated [18, 19]. Compared to conventional hollow rectangular waveguides, they generally have advantages such as planar fabrication, lower manufacturing cost, and lower loss for millimeter wave and microwave applications, to name a few. A general layout of the gap waveguide has been depicted in Fig. 18(a). The height of the air gap is set to be less than quarter wavelength so that for the PEC-PEC (perfect electric conductor) region, only the TEM mode is permitted to propagate, while for the PEC-PMC (perfect magnetic conductor) region, no wave will be allowed to propagate since all modes are under cutoff. In this sense, a quasi-TEM mode wave is confined and propagates in the air gap only in the center PEC-PEC region. One limitation is that this gap waveguide can only support electric field vertical to the plates since it is based on the parallel plate mode. However, this gap waveguide will not support horizontal electric field (parallel to the plates), when the center PEC-PEC region is unbounded. The metamaterial based PMCs used in gap waveguide also require vias in the mushroom type [20], or are implemented with a bed of nails [19].
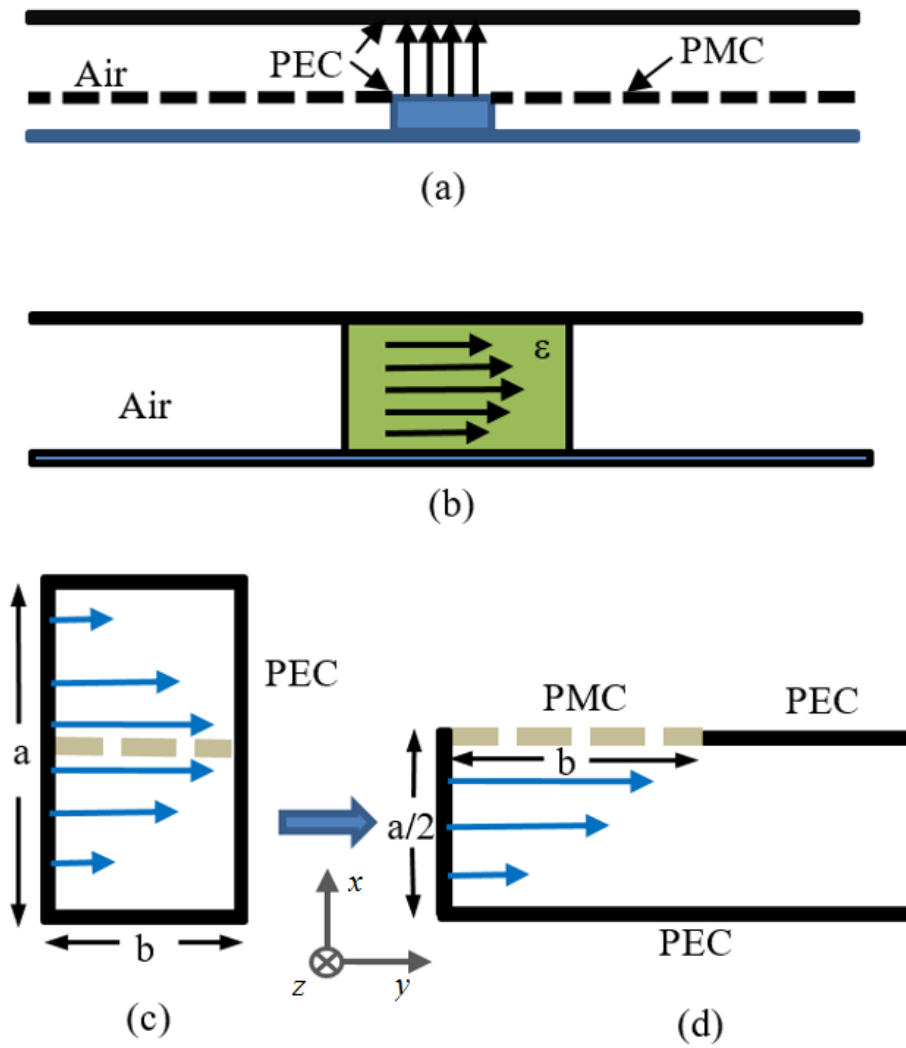
Figure 18   (a) Structure and electric field distribution of gap waveguide. (b) Structure and electric field

distribution of NRD. (c) Structure of a typical hollow rectangular waveguide and its dominant TE10 mode E

field distribution. Dash line stands for equivalent PMC boundary (d) Structure of a PMC-PEC waveguide

with the half dimension and half mode distribution.

One well-known structure that will support a mode with horizontal electric field is the

non-radiative dielectric waveguide (NRD) [21] as shown in Fig. 18(b). To construct the NRD

waveguide, a dielectric block is used between two parallel metal plates with a distance smaller than half wavelength. Due to the dielectric constant of the dielectric block, waves are below cutoff and are able to propagate along the block. The dominant TM mode has almost all horizontal electric field distribution inside the dielectric. However, the region outside of the dielectric is under cutoff for anypolarized horizontally mode, which means no appreciable propagation will occur, and thus the mode is confined. There also exists some edge field in the discontinuity of air and dielectric that is bent to the metal plate or radiate outside which can be further utilized as leaky wave antenna [22]. The limitations for NRD are also obvious. One needs to place a bulky dielectric in between the metal plates which could make it a heavy structure and hard to engineer. Excitation can also be a problem for NRD waveguide.

In this chapter, we utilize a rectangular waveguide mode with a horizontal polarization, as shown in Fig. 18 (c), as our main mode of propagation. But instead of using a complete rectangular waveguide to propagate its dominant mode (say TE_{10} mode), we use a PMC wall to truncate the structure dimension as well as the original TE_{10} mode into half as shown in Fig. 18 (d). Thus, this mode profile resembles that shown in the lower half structure of Fig. 18 (c), as so called half TE_{10} mode. The PMC is realized with a metasurface type structure, which is for horizontal polarization. Moreover, as shown in Fig. 18 (d), the side-wall of the guide is open, but the mode is mainly confined, as the horizontal polarized mode is under cut-off in the neighboring PEC-PEC region. Thus, the whole structure can be regarded as the reverse of the gap waveguide. We use the PMC-PEC region to confine and propagate the horizontally polarized mode, while using the PEC-PEC region as a cut-off region of the

dominant mode. As noted earlier, the reverse occurs in the gap waveguide. Thus, a difference from the gap waveguide is that this structure supports horizontal electric field propagation instead of the parallel plate quasi-TEM mode with vertical electric field. The PMCs are also realized with simple periodic traces on a conductor backed dielectric.

Compared to the NRD waveguide, this PMC-PEC waveguide has only air gap in between, and compared to the metamaterial gap-waveguide, it does not require vias or pins, thus making this structure much easier to manufacture. Excitation is also simple, one can just simply use a probe to couple field into the waveguide as will be discuss in the fabrication section.

2.2 Principle of Operation

Consider a hollow rectangular waveguide cross section with longer dimension *a* and shorter dimension *b* as shown in Fig.16 (c). The guided wave is completely bounded by PEC walls so that for TE_{10} mode, the electric field is shorted to zero at the two ends of the longer dimension. However, equivalent field distribution should be achieved when we place a PMC wall in the middle of the waveguide, as the boundary conditions are met. Accordingly, one can make a half TE_{10} mode waveguide with PEC and PMC walls in parallel, as also shown in in Fig. 18 (d). For this mode, the cut-off frequency is linked to the distance between PMC and PEC walls *h=a/2*:

$$f_{c1} = \frac{1}{2a\sqrt{\mu\epsilon}}.\qquad\qquad(2.1)$$

However, for the PEC-PEC region next to this PMC-PEC region in Fig. 18 (b), the

cut-off frequency for TE$_{10}$ mode is:

$$f_{c2} = \frac{1}{2h\sqrt{\mu\epsilon}} = \frac{1}{a\sqrt{\mu\epsilon}}. \qquad (2.2)$$

which is quite above the cut-off for the PMC-PEC region. Therefore, in theory, for frequencies greater than f_{c1} but smaller than f_{c2}, this half TE$_{10}$ like mode can only exist in the PMC-PEC region. The right side of PEC-PEC region can be opened at the right end compared to Fig. 18 (c), in which the structure is not closed from for the right side. Nevertheless, as the PEC-PEC region is cutoff, no mode with horizontal electric field may exist.

But note that similar to the NRD case (Fig. 18 (b)), there is in fact chance for the field to bend toward the PEC board at the PMC edge (fringe). This can potentially couple energy to the PEC-PEC region due to the discontinuity in the transverse direction. The PEC-PEC region will always support parallel plate TEM mode from DC. If the parallel plate region is terminated with an open end, it will radiate out to free space at the end. In the application section, we utilize this property to construct a type of leaky wave antenna.

2.3 Design of PMC Wall

The PMC region of the top wall is a key part in the designing of this waveguide. This PMC region can be made in a metasurface approach, showing a magnetic response for horizontal polarized field. Here we use simple constituent subwavelength metal strips placed periodically on a PEC backed substrate, as was done in [7]. A unit cell for the PMC is depicted in Fig. 19 (a). For a given substrate (say Rogers RT 6010), we carefully choose the

unit cell periodicity and top metal strip width to adjust the phase of reflection coefficient to approach zero.

Here, we aim our design at X-band. The unit cell periodicity is $d_y = 1.5$mm. A strip of width W=1.2 mm is oriented along x on the Rogers 6010 substrate with relative dielectric constant of 10.2 and loss tangent 0.002, backed by copper. The thickness of the dielectric h is 1.9 mm.

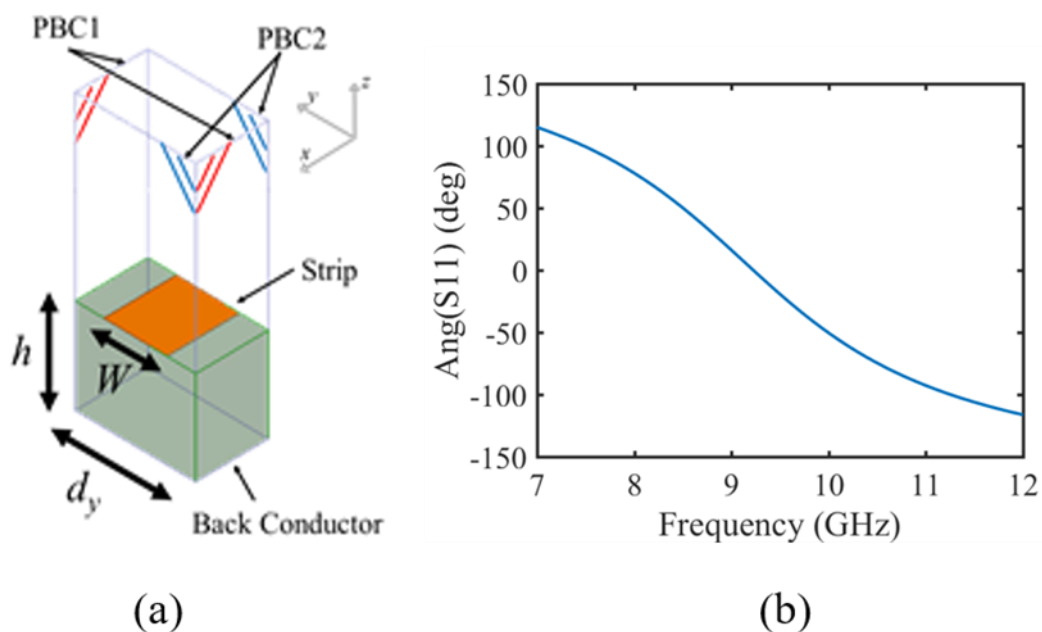Figure 19   (a) Unit cell simulation of PMC using periodic boundary condition (PBC).   (b) phase angle

of S11 for Floquet port simulation

Periodic boundary conditions are placed in the sides and a Floquet port is placed in the top to measure the reflection phase in the periodic unit-cell simulation. The phase of the reflection coefficient for this unit cell is shown in Fig. 19 (b). For frequencies around 9 GHz

where the phase angle of S_{11} for TE wave (electric field perpendicular to metal width and parallel to substrate surface) approaches 0 degrees, the surface can be approximated as a PMC. Note that PMC is usually a narrow band structure and the PMC working frequency cannot deviate too much from 9GHz. The slope of the curve shows a reasonable range of frequencies over which the PMC response can be achieved.

2.4 Waveguide Dispersion Characteristics

Another key parameter in the designing of this PMC-PEC waveguide is the distance H between the PMC and PEC walls since this distance determines the cut-off frequency of the dominant mode (half TE_{10} like mode). Here we specify H to be 7.9mm to fit the PMC working frequency. A simulation setup of the main waveguide structure is performed in Ansys HFSS. The waveguide structure is shown in Fig. 20.
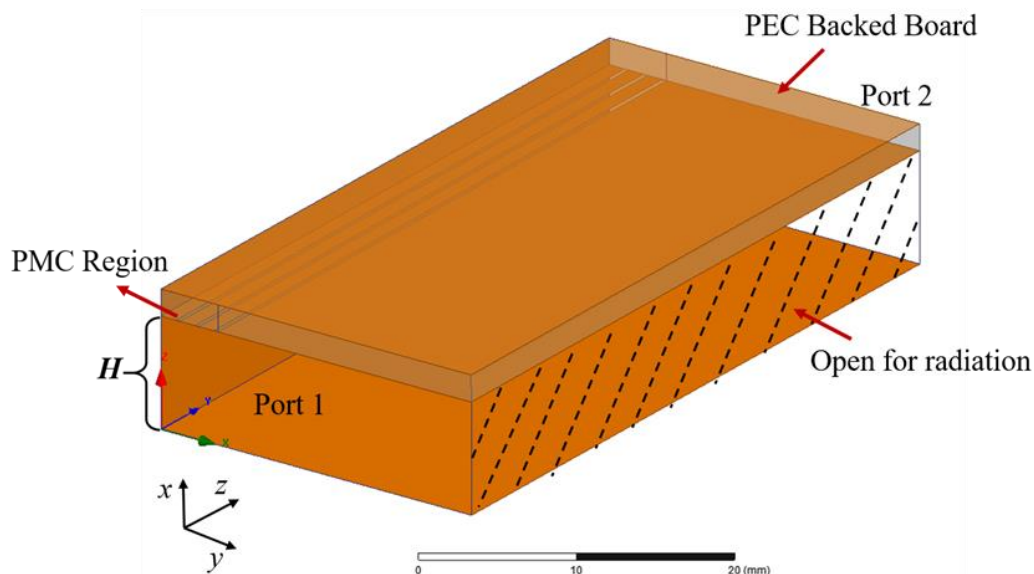
Figure 20   PMC-PEC waveguide structure. PEC regions and strips of PMC are colored with orange.

The PMC region in the top wall is composed of multiple strips placed on the grounded substrate. The remainder of the top wall has a solid metal, and thus acts as a PEC. The dimensions of strips were discussed in section 2.3. The waveguide length in the z-direction is set to be 50 mm. The right side of the whole structure is open for radiation.

Figure 21   Dispersion diagram of PMC-PEC Waveguide. Normalized wavenumber (blue dashed curve) with respect to axis on the left, and normalized leakage (red solid curve) with respect to axis on the right.

After solving the port modes, the dispersion diagram for the propagating mode can be found as depicted in Fig. 21.
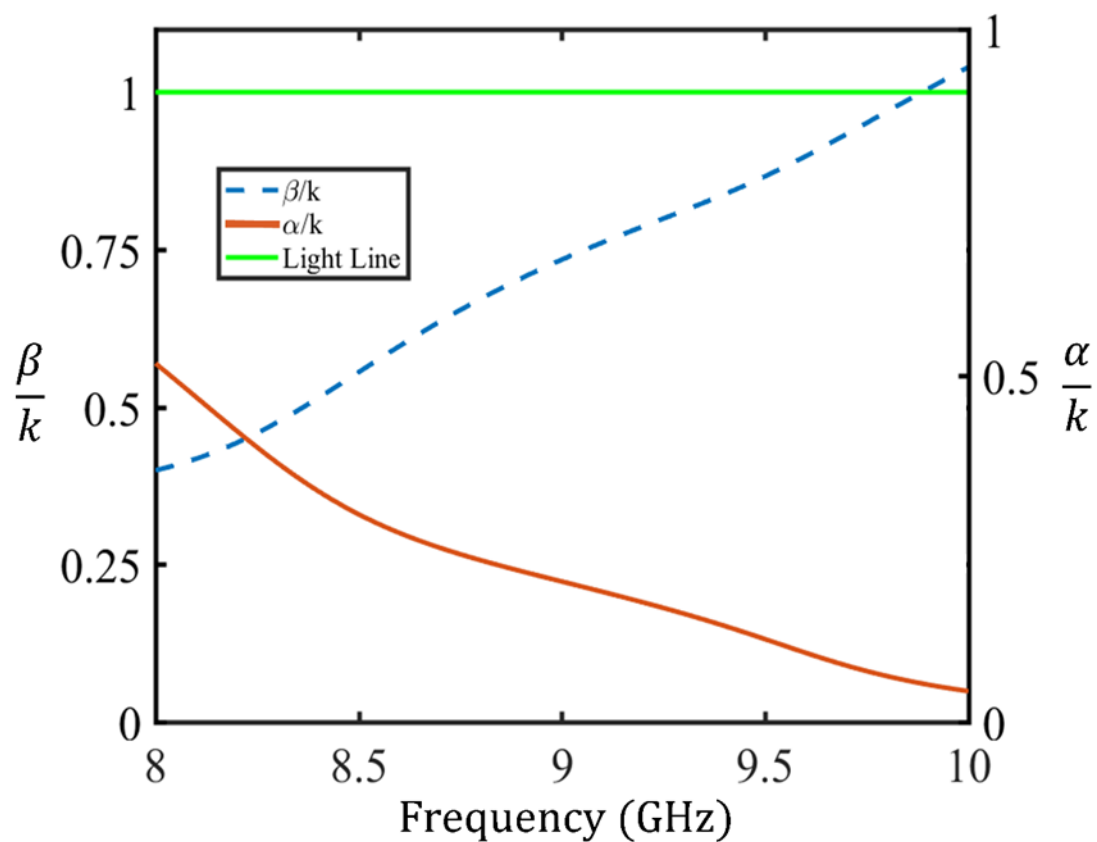
From this dispersion diagram, we can see that from 8.5GHz to 9.5GHz, $\beta < k_0$ (where k_0 is the free space wave number) is always valid, and hence it remains as a fast-wave structure for the PMC working range. From Fig. 21, we can also see the attenuation constant of the waveguide. Although some of the loss is due to lossy substrate and lossy PMC region, yet most part of the loss comes from the field coupled to the PEC-PEC region and radiating away to free space, i.e. a leaky wave. One can utilize this radiation loss for the application of leaky wave antennas.

2.5 Application of Leaky Wave Antenna

A leaky wave antenna is based on a guiding wave structure with some continuous or periodic discontinuity that permits leakage of power from a fast wave along the propagation in the waveguide [23, 24]. For a fast wave in leaky wave antenna, some of the field will leak out to form a far field pattern. The beam direction is given by:

$$\sin(\theta_{max}) = \frac{\beta}{k_0}. \qquad (2.3)$$

Here θ_{max} is the main beam angle measured from the broadside direction. Related with axes in Fig. 18, this pattern should be in y-z plane, and the beam direction refers to x axis, i.e. $\varphi = \theta_{max}$ for beam angle. Thus, for PMC working frequency at around 9 GHz, we can see from Fig. 21 that β/k_0 equals to 0.7341, meaning the main beam angle θ_{max} should

35

locate at 47⁰ according to equation (2.3).

A wave port simulation with excitation for the PMC-PEC waveguide is then carried out in HFSS. The top view is shown in Fig. 22. The structure still follows the dimension discussed in section 2.4, except that a coaxial probe now excites the waveguide.
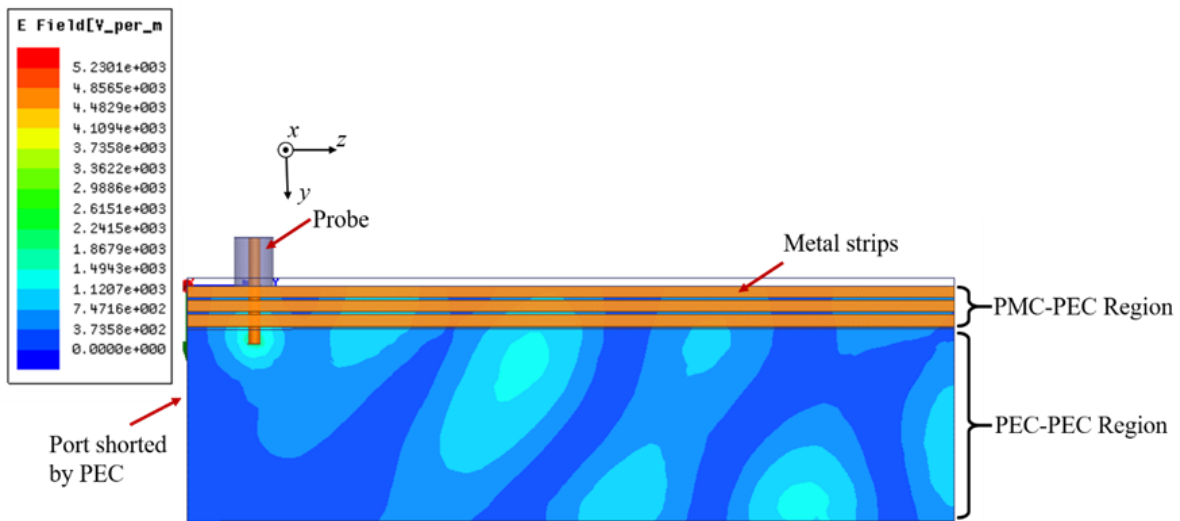
Figure 22　Full wave simulation for PMC-PEC waveguide with probe (top view)

We place the probe close to the PMC board (2mm distance) to achieve strong electric field, since in this propagating mode, electric field should achieve maximum value along PMC region. Meanwhile, we use a PEC to short one port of the waveguide only to allow radiating from the end or in the PEC-PEC region. This short PEC wall is set to be quarter wavelength away from the probe.

The electric field distribution is also shown in Fig. 22. When the field is coupled into the

waveguide, part of the wave is confined and propagates along the PMC-PEC waveguide region. Clearly there is part of wave leaking into PEC-PEC region and finally leaking out to free space in a certain angle oblique to the mode propagating direction. At the end, 75% of the total power is radiated along this 50mm long waveguide. This proposed PMC-PEC LWA was then fabricated through printed circuit board (PCB) process. For PMC board fabrication, we used the same board (Rogers RT 6010) as in simulation.

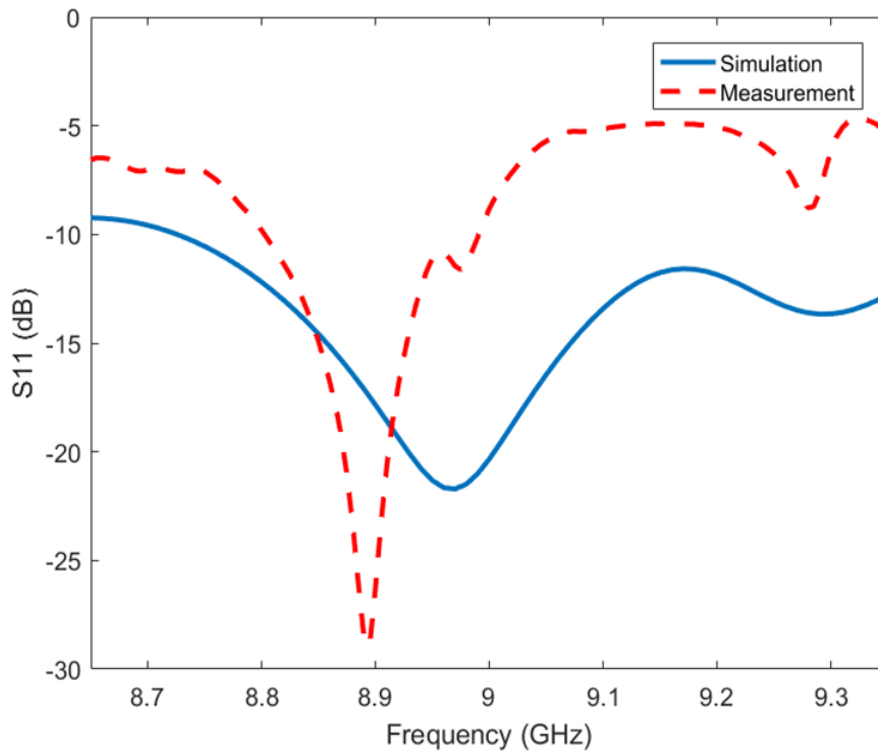Figure 23   Measured (dash line) S11 and simulated (solid line) S11

Both measured and simulated S_{11} parameters are shown in Fig. 23. It can be observed that the measured S_{11} is below -10 dB from 8.82GHz to 9GHz, which is narrow band as

expected. Both curves agree well except there is less than 0.1GHz resonant frequency shift. This resonance shift may come from the slight difference of dielectric constant between the board we simulated and the board we fabricated with.

The PMC-PEC LWA is also tested in an antenna chamber to measure the far-field patterns. Fig. 24 shows the pattern of this LWA at 8.85GHz. This pattern indicates an oblique beam in y-z plane (H-plane in this scenario) for both simulation and measurement. For simulation, the main beam angle is $\varphi=48.25^{\circ}$, while for measurement it locates on $\varphi=50^{\circ}$. This discrepancy may come from the angle sampling in the pattern measurement. Theoretically, for 8.85GHz we can find out the propagation constant of the waveguide according to dispersion diagram in Fig. 21. Using equation (3), we can calculate the approximated main beam angle 44°, which is close to both simulation and measurement results.
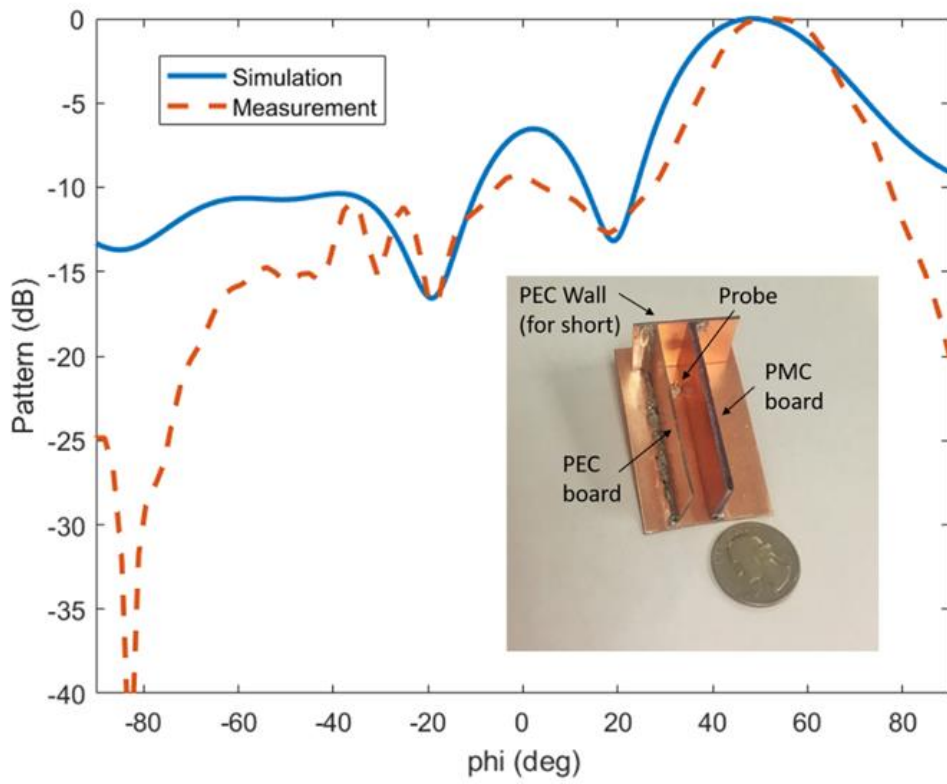
Figure 24   Measured (dash line) and simulated (solid line) radiation pattern and fabricated PMC-PEC

waveguide LWA.

CONCLUSION

In this thesis, first a non-periodic approach for tailoring the scattering of metasurfaces for blazing (retro-reflection) and beam-splitting is investigated. The phase response for single elements is characterized for building up the far-field pattern. Genetic Algorithm is used to optimize a simple theoretical array model of the scattering scenario, to reduce the first side lobe level of the backscattered beam, as well as splitting of scattered beams into two desired angles. Additional phase constraints can be applied into this optimization strategy considering the limitations of the practical element utilized. Two metasurface samples are fabricated to demonstrate blazing effect. The main beam at retro-reflection angle is observed which matches simulation results as well as a suppressed specular beam is achieved.

In the second chapter, a metasurface assisted PMC-PEC leaky waveguide structure is proposed. In the guiding wave region, this waveguide can support half of TE_{10} mode with compact size through simple probe excitation. Realization of the PMC wall without vias, and dispersion characteristics of the guide are discussed. Finally, we apply this PMC-PEC waveguide to the design of leaky wave antenna achieving a main radiation beam in oblique angle.

REFERENCE

[1] C. Holloway, E. Kuester, J. Gordon, J. O'Hara, J. Booth and D. Smith, "An Overview of the Theory and Applications of Metasurfaces: The Two-Dimensional Equivalents of Metamaterials", *IEEE Antennas and Propagation Magazine*, vol. 54, no. 2, pp. 10-35, 2012.

[2] A. Kildishev, A. Boltasseva and V. Shalaev, "Planar Photonics with Metasurfaces", *Science*, vol. 339, no. 6125, pp. 1232009-1232009, 2013.

[3] S. Tretyakov, "A personal view on the origins and developments of the metamaterial concept", *Journal of Optics*, vol. 19, no. 1, p. 013002, 2016.

[4] D. Smith, J. Pendry, and M. Wiltshire, "Metamaterials and Negative Refractive Index", *Science*, vol. 305, no. 5685, pp. 788-792, 2004.

[5] N. Yu and & F. Capasso, "Flat optics with designer metasurfaces," Nature materials, vol. 13, pp. 139-150, Jan. 2014.

[6] S. Tretyakov and S. Maslovski, "Thin absorbing structure for all incidence angles based on the use of a high-impedance surface", *Microwave and Optical Technology Letters*, vol. 38, no. 3, pp. 175-178, 2003.

[7] X. Li, M. Memarian, K. Dhwaj, T. Itoh, "Blazed metasurface gratings: Planar equivalent of sawtooth gratings", IEEE Intl Microwave Symp., May 2016

[8] M. Memarian, X. Li, Y. Morimoto and T. Itoh, "Wide-band/angle Blazed Surfaces using Multiple Coupled Blazing Resonances", *Scientific Reports*, vol. 7, p. 42286, 2017.

[9] C. Tao, M. Memarian, Y. Morimoto, T. Itoh, "Non-periodic Metasurfaces for Blazing and

Beam Splitting", IEEE Asia/Pacific Microwave Conference (APMC), 2016.

[10] T. Itoh and R. Mittra, "An analytical study of the echelette grating with application to open resonators," Microwave Theo. Tech., IEEE Trans., vol. 17, pp. 319-327, Jun. 1969.

[11] A. Hessel, J. Schmoys, and D. Y. Tseng, "Bragg-angle blazing of diffraction gratings," Jounral of Optical Society of America, vol. 65, pp. 380-384, 1975.

[12] Jull, E. V., J. W. Heath, and G. R. Ebbeson. "Gratings that diffract all incident energy," Jounral of Optical Society of America, vol. 67, pp. 557-559, 1977.

 [13] A. L. Kitt, J. P. Rolland, and A. N. Vamivakas, "Visible metasurfaces and ruled diffraction gratings: a comparison," Opt. Mater. Express, vol. 5, pp. 2895-2901, 2015

[14] M. Memarian, X. Li, T. Itoh, "Resonant Blazed Metasurface Gratings," IEEE European Microwave Conference (EUMC), 2016.

[15] J. S. Sun, D. S. Goshi, & T. Itoh. "Optimization and modeling of sparse conformal retrodirective array". IEEE Transactions on Antennas and Propagation, 58, pp. 977-981, 2010.

[16] H. Li, B. Wang, L. Guo, W. Shaoand and P. Du, "A Far Field Pattern Analysis Technique for Reflectarrays Including Mutual Coupling Between Elements", *Journal of Electromagnetic Waves and Applications*, vol. 23, no. 1, pp. 87-95, 2009.

[17] K. Wang, J. Zhao, Q. Cheng, D. Dong and T. Cui, "Broadband and Broad-Angle Low-Scattering Metasurface Based on Hybrid Optimization Algorithm", *Scientific Reports*, vol. 4, 2014.

[18] P. Kildal, E. Alfonso, A. Valero-Nogueira and E. Rajo-Iglesias, "Local

Metamaterial-Based Waveguides in Gaps Between Parallel Metal Plates", IEEE Antennas and Wireless Propag. Lett., vol. 8, pp. 84-87, 2009.

[19] P. Kildal, A. Zaman, E. Rajo-Iglesias, E. Alfonso and A. Valero-Nogueira, "Design and experimental verification of ridge gap waveguide in bed of nails for parallel-plate mode suppression", *IET Microwaves, Antennas & Propagation*, vol. 5, no. 3, p. 262, 2011.

[20] E. Pucci, E. Rajo-Iglesias and P. Kildal, "New Microstrip Gap Waveguide on Mushroom-Type EBG for Packaging of Microwave Components", IEEE Microwave and Wireless Components Letters, vol. 22, no. 3, pp. 129-131, 2012.

[21] T. Yoneyama and S. Nishida, "Nonradiative Dielectric Waveguide for Millimeter-Wave Integrated Circuits", IEEE Trans. *Microw. Theo. Techn*., vol. 29, pp. 1188-1192, 1981.

[22] A. Sanchez and A. Oliner, "A New Leaky Waveguide for Millimeter Waves Using Nonradiative Dielectric (NRD) Waveguide-Part I: Accurate Theory", IEEE Trans. *Microw. Theo. Techn*., vol. 35, pp. 737-747, 1987.

[23] D. Jackson, C. Caloz and T. Itoh, "Leaky-Wave Antennas," Proc. IEEE, vol. 100, no. 7, pp. 2194-2206, 2012.

[24] M. Memarian and G. V. Eleftheriades, "Dirac leaky-wave antennas for continuous beam scanning from photonic crystals", *Nature Communications*, vol. 6, p. 5855, 2015.